Experimental and numerical investigation of nonlinear diffraction wave loads on a semi-submersible wind turbine

Haoran Li [a, *], Erin E. Bachynski [a, b]

[a] Department of Marine Technology, Norwegian University of Science and Technology (NTNU) Trondheim, Norway
[b] Centre for Autonomous Marine Operations and Systems (AMOS), NTNU, Trondheim, Norway

ARTICLE INFO

ABSTRACT

In a severe sea state, nonlinear wave loads can excite resonant responses of floating wind turbines either at high (structural) or low (rigid body motions) natural frequencies. In the present work, a computational fluid dynamics (CFD) model and an engineering model based on potential-flow theory with Morison-type drag are developed to investigate nonlinear wave loads on a stationary, rigid semi-submersible wind turbine under regular and irregular waves. The numerical results are validated against experimental measurements. A trimmed floater is modelled to examine the change in nonlinear wave loads due to the mean pitch angle which occurs during operation of a floating wind turbine. Furthermore, wave loads on each column are investigated numerically. Compared to the experimental measurements, the CFD model gives better estimations than the engineering model for the first, second and third order wave diffraction loads. The engineering model based on the first- and second-order potential-flow theory has large discrepancies in the phase of high order wave diffraction loads and underpredicts the amplitude of low-frequency wave loads. In the CFD simulations for the studied wave period (12.1 s), the second and third harmonic surge forces on the starboard columns are significantly larger than those on the upstream column, while first harmonic results are consistent with potential flow. The trim angle (5°) results in an increasing surge force and pitch moment but a decreasing heave force.

© 2021 The Author(s). Published by Elsevier Ltd. This is an open access article under the CC BY license (http://creativecommons.org/licenses/by/4.0/).

1. Introduction

Recently, there has been a huge increase in the use of wind turbines for generating electricity. To access a larger wind resource and reduce visual and acoustic pollution, a growing number of offshore wind turbines (OWTs) has been installed in recent years. In shallow and intermediate water depths, bottom-fixed OWTs are employed. However, in deep water, the costs of bottom-fixed foundations rise sharply, so a wide variety of floating wind turbine (FWT) concepts have been proposed, such as spar, semi-submersible and tension leg platforms (TLP). With increasing water depth, FWTs may be exposed to harsh environments and steep waves which induce highly nonlinear wave loads on the floater of FWTs. The high-frequency loads can cause springing and ringing, while the low-frequency loads can lead to the resonance in surge, sway and yaw of a moored platform. Mercier et al. [1] showed the

importance of high order wave loads on TLPs through experiments. Coulling et al. [2] also used experiments and numerical tools to stress the importance of second-order difference-frequency wave forces in capturing the global response of a semi-submersible FWT. As the responses of FWTs are largely affected by nonlinear wave loads, validated modelling tools should be developed to predict these loads more accurately while keeping the computational efficiency at a reasonable level.

Most of the investigations of nonlinear hydrodynamic loads on different types of wind turbines are based on low order potential flow models [3—7]. This limits hydrodynamic modeling to linear or weakly nonlinear models and may be less reliable for analysis of FWTs in extreme condition. Some studies use high order commercial or in-house CFD codes to investigate wave loads and motion responses on various types of FWTs, as summarized in Table 1.

Although the offshore oil and gas industry has demonstrated the long-term survivability of semi-submersible platforms and can provide some guidelines for design, significant differences exist. With a smaller payload and no permanent residences for personnel, FWTs are significantly smaller than oil and gas platforms

* Corresponding author. Otto Nielsens veg 10, Marine Technology Centre, 2nd floor, Trondheim, 7491, Norway.
E-mail address: haoran.li@ntnu.no (H. Li).

Table 1
Overview of investigations of FWTs using CFD.

Reference	Methods	Conditions	Main conclusions
Beyer et al. [8]	1. RANS equation 2. VOF for free surface 3.SST turbulence model 4. Multi-body system for calculating motion	Surge free decay test of OC3 spar-buoy wind turbine in still water	Pitch motion was excited due to vortex-induced forces on the platform
Benitz et al. [9,10]	1. RANS equation 2. VOF for free surface 3. Spalart-Allmaras turbulence model 4. Wave2Foam for wave	Hydrodynamic loads on OC4 semi-submersible platform under current-only and wave-only conditions	Shadowing effects and transverse forces from vortex shedding can be captured.
Rivera-Arreba et al. [11]	1. NS equation 2. VOF for free surface 3. Laminar flow 4. Wave2Foam for wave	Heave and pitch free decay and responses of OC5 semi-submersible platform under heave resonance and large steepness wave conditions	For free decay cases, the heave response of the potential-flow model showed an amplitude 40% lower than CFD model. However, the heave responses under different regular waves were slightly lower in CFD model.
Nematbakhsh et al. [12−14]	1. One-fluid NS equation. 2. Level set method for free surface 3. Laminar flow 4. The loads from structural model are included in NS equation.	Surge and heave free decay tests and responses of TLP wind turbine under regular wave condition	The chance of strong vortex shedding behind the TLP is small due to the large diameter of the TLP tank and the small Keulegan−Carpenter (KC) number. A higher mean surge motion is noticed due to better representation of nonlinear effects.
Hu and Liu et al. [15,16]	1. CIP method [17] 2. THINC [18]for free surface 3. ImmersedBoundary Method for fluid-structure interaction	Surge, heave and pitch RAO of two types of semi-submersible wind turbines	CFD simulations can study the nonlinear phenomena in large amplitude wave conditions.

[19]. Semi-submersible FWTs are usually made of three or four vertical columns connected by cross braces which affect the flow regimes around columns. In addition, heave plates are often attached to the bottom of the columns to increase the added mass and damping. An additional lift force on heave plates due to vortex shedding may also appear [10]. Another difference between FWTs and oil and gas platforms is a mean pitch angle for the wind platform during operation due to the aerodynamic thrust force.

To better understand the nonlinear diffraction wave loads on a semi-submersible FWT, a CFD model and a potential flow theory model are used to simulate the interaction of a semi-submersible FWT with regular and irregular waves. The numerical results are compared with experimental data. Higher order sum-frequency wave loads are examined for a regular wave condition; an irregular wave state is chosen to investigate the wave loads around natural periods of rigid body motions. Because a fixed platform is considered here, we cannot directly compare responses around low frequencies. However, some qualitative conclusions are also drawn from the results.

A trimmed condition under regular wave is also modelled to examine the change of nonlinear wave loads due to the trim induced by the mean aerodynamic thrust force. In addition, wave loads on each column are extracted to better understand the effects of the multimember arrangement of the semisubmersible.

Section 2 briefly describes the experiment for comparison, while Section 3 describes the CFD and potential flow theory models. In Section 4, the wave loads on the upright and trimmed floater under regular wave condition are analyzed. Then, the wave loads due to irregular waves are examined. Finally, conclusions are presented in Section 5.

2. Review of experiment

In the present work, experimental results for the wave loads on the floater are from Phase I of the Offshore Code Comparison Collaboration, Continued, with Correlation, and unCertainty (OC6) project [20]. The model test was performed in the concept basin of the Maritime Research Institute Netherland (MARIN). The geometry of the floater corresponds to the DeepCwind semi-submersible floater [21] at 1:50 scale. The right-handed coordinate system used in this research originates at the center of the main column at the still water line, with positive x being in the direction of propagating waves, and z being up. The tower of the wind turbine was removed and the floater was attached to the carriage through a frame, as shown in Fig. 1. Wave loads on the stationary model were measured using a six-component gauge connecting the floater and the frame. The results presented in this paper are calculated based on the shown coordinate system. All data and results are given at full scale, except when explicitly mentioned. The uncertainty in the experiment is about 2% for the measured force and 5% for the measured moments [20].

One regular wave with height $H = 7.1$ m and period $T = 12.1$ s, and an irregular wave with significant wave height $H_s = 7.1$ m and peak period $T_p = 12.1$ s were selected for this research. The irregular wave was generated based on the JONSWAP spectrum with the peak enhancement factor equal to 3.3.

3. Computational model

The same global coordinate system as in the experiment (Fig. 1) is implemented in the computational model.

3.1. CFD model

The multiphase interFoam solver of OpenFOAM [22] is a fully nonlinear Navier-Stokes/VOF solver. Extending the interFoam solver with the wave generation and absorption toolbox, waves2Foam, developed by Jacobsen et al. [23], generates the waveFoam solver. Furthermore, a fully nonlinear potential flow solver, Oceanwave3D [24], is coupled with the waveFoam solver to minimize numerical diffusion and reduce the computational time for the irregular wave case [25].
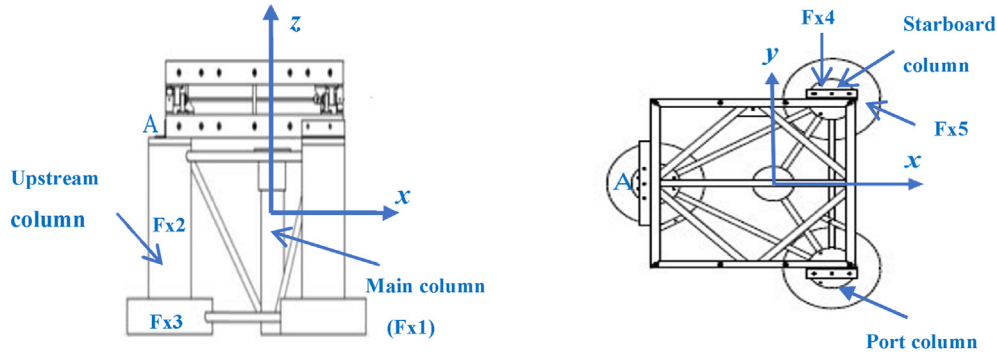
Fig. 1. Side (left) and top (right) view of the constrained model [20].

3.1.1. Governing equations

The waveFoam solver utilizes the two-phase incompressible Navier-Stokes equations to compute the fluid flow around the stationary semi-submersible. The governing equations consist of mass conservation and momentum conservation:

$$\frac{\partial u_i}{\partial x_i} = 0 \tag{1}$$

$$\frac{\partial \rho u_i}{\partial t} + \frac{\partial \rho u_j u_i}{\partial x_j} = -\frac{\partial p^*}{\partial x_i} + F_{b,i} + \frac{\partial}{\partial x_j}\left[\mu_{eff}\frac{\partial u_i}{\partial x_j}\right] \tag{2}$$

where u_i $(i = x, y, z)$ are the fluid velocity in Cartesian coordinates, ρ is the fluid density, p^* is pressure in excess of the hydrostatic pressure, F_b is an external body force including gravity and μ_{eff} is the effective dynamic viscosity. For laminar flow, μ_{eff} is equal to the laminar dynamic viscosity. For turbulent flow, it should include turbulent dynamic viscosity $\rho\nu_t$.

The local density ρ and the effective dynamic viscosity μ_{eff} are defined by the volume fraction α which is bounded between 0 (air) and 1 (water). The turbulent dynamic viscosity $\rho\nu_t$ is neglected in laminar flow model.

$$\rho = \alpha\rho_{water} + (1-\alpha)\rho_{air} \tag{3}$$

$$\mu_{eff} = \alpha\mu_{water} + (1-\alpha)\mu_{air} + \rho\nu_t \tag{4}$$

The air-water interface is tracked by the volume of fluid VOF method [26] in OpenFoam. The volume fraction is advanced in time once the velocity is known, following scalar advection equation:

$$\frac{\partial \alpha}{\partial t} + \frac{\partial u_i \alpha}{\partial x_i} + \frac{\partial u_{r,i}\alpha(1-\alpha)}{\partial x_i} = 0 \tag{5}$$

The smearing of the interface is vastly reduced by the introduction of the artificial velocity u_r. It is only active in the vicinity of the interface where $0 < \alpha < 1$, see Berberovic et al. [27] for details. To ensure the boundedness of solution, a multi-dimensional flux limited scheme (MULES) is applied. To identify the free surface elevation, the volume fraction α is integrated along a vertical line around the air-water interface.

3.1.2. Turbulence modelling

The effects of turbulence are incorporated in the governing equations by using different transport equations to calculate the turbulent kinematic viscosity ν_t. The $k - \omega$ SST turbulence model has shown good results for simulating two-phase flow and predicting wave elevation [28,29] and is applied in this paper. The incompressible $k - \omega$ SST model for a single fluid is a two-equation model and is given in OpenFoam as:

$$\frac{\partial k}{\partial t} + \frac{\partial u_j k}{\partial x_j} - \frac{\partial}{\partial x_j}\left[(\nu + \sigma_k \nu_t)\frac{\partial k}{\partial x_j}\right] = P_k - \beta^* \omega k \tag{7}$$

$$\frac{\partial \omega}{\partial k} + \frac{\partial u_j \omega}{\partial x_j} - \frac{\partial}{\partial x_j}\left[(\nu + \sigma_\omega \nu_t)\frac{\partial \omega}{\partial x_j}\right] = \frac{\gamma}{\nu_t}G - \beta\omega^2$$
$$+ 2(1 - F_1)\frac{\sigma_{\omega 2}}{\omega}\frac{\partial k}{\partial x_j}\frac{\partial \omega}{\partial x_j} \tag{8}$$

where k is the turbulent kinetic energy, P_k is the production term of k, ν is kinematic viscosity, ν_t is the turbulent kinematic viscosity, ω is the specific dissipation rate, as described in detail by Menter et al. [30]. In the present work, to avoid significant wave damping induced by increasing turbulent viscosity [31,32], a modified waveFoam solver is built to explicitly consider the variable density in the $k - \omega$ SST model [32].

Table 2 shows the Keulegan-Carpenter (KC) and Reynolds numbers at model scale, assuming the wave is fully linear. The inflow velocity is the maximum horizontal water particle velocity. The KC number is around 1 for most of components. Hence, weak vortices are expected in the experiment and CFD simulations. Although the Reynolds numbers are on the order of 10^4-10^5, previous studies considering the same geometry suggest that the turbulence model is not essential for the CFD simulations due to the low KC number of upper column and heave plate [33]. For regular wave cases, simulations using both laminar (L.F) and turbulent (T.F) flow are carried out for comparison.

3.1.3. Numerical domain

To reduce the computational time, CFD simulations with a stationary semi-submersible floater were carried out at model scale (1:50). In this section, all data are given at model scale.

The width (3.72 m) and water depth (3.6 m) of the experimental wave flume are modelled. The numerical wave tank (36 m) is shorter than the experimental wave flume, but long enough to dissipate the reflected waves. Fig. 2 shows good agreement in the overlayed wave elevation at the center of floater for three cycles separated in time: before reflections can reach the center of the floater, after reflections from the outlet are expected, and after reflections from both inlet and outlet are expected. The height of

Table 2
KC and Reynolds numbers for different parts of floater for regular wave realization (model scale).

	Main column	Upper column	Heave plate	Cross brace
KC ($-$)	2.89–3.43	1.86	0.93	13.94
Re ($\times 10^5$)	0.33–0.40	0.62	1.23	0.08
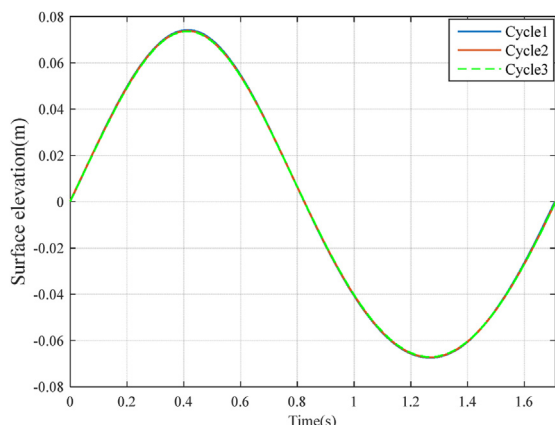
Fig. 2. Surface elevation at the center of floater at different times, no semi-submersible present (Cycle1: only incident wave. Cycle2: incident wave with reflected wave from outlet boundary. Cycle3: incident wave with reflected wave from inlet and outlet boundaries).

the air regime is set to 1 m. Fig. 3 shows a plan view of the numerical wave tank with floater.

After spatial discretization, the size of a cell in all directions is 0.12 m. Thereafter, for the air-water interface, the mesh was refined. A mesh convergence study for free surface elevation and calculated wave loads was carried out. In Table 3, the wave height at origin (center of floater) is compared to the specified wave height at inlet (H = 0.142 m) and the wave loads are compared to those with the finest mesh size (Level 4) for three different spatial discretizations. The 3-3 level of refinement, resulting in a mesh size of 0.015 m ($\approx H/10$), is applied for the air-water interface and surface of columns. Around the cross braces, which have a smaller diameter, the 4-4 level is applied, leading to cross brace mesh size 0.0075 m ($\approx H/20$). This local refinement allows for a high-resolution interface while keeping the total number of computational cells relatively low. For the turbulent flow model, 25 cell layers adjacent to the floater surface are generated. The thickness of the first layer is 2.0 μm and its expansion ratio is 1.2.

3.1.4. Boundary conditions

In the Navier-Stokes/VOF solver, boundary conditions are imposed on all surfaces in the numerical domain. The general denomination of boundary surfaces is given in Fig. 4.

The velocity and the volume fraction boundary conditions are given by stream function wave theory at the inlet and a constant current with zero velocity at the outlet. The floater surfaces and tank bottom are modelled as fixed walls. For the laminar flow model, a slip condition is applied, which means the effect of viscosity and turbulence generation are neglected. For the turbulent flow model, wall functions are applied for k (1e-5 m^2/s^2) and ω (1.0 1/s). A continuous wall function based on Spadling's law [34] is implemented for the turbulent viscosity. Furthermore, a Dirichlet boundary condition is set for the velocity while a Neumann condition is used for pressure and volume fraction on the fixed walls. A slip condition is applied to the front and back walls. At the atmosphere boundary, the total pressure is set to zero and an atmospheric boundary condition is applied for the velocity and volume fraction. This means that air and water are allowed to leave the numerical domain, while only air is allowed to flow back in.

The Waves2Foam toolbox [23] implements relaxation zones (blue part in Fig. 4) to avoid wave reflection from the outlet boundary (II) and to prevent internally reflected waves (I). Rectangular relaxation zones are defined in this work, as in Bruinsma's work [35].

3.1.5. Temporal discretization

To ensure numerical stability, the temporal discretization is determined based on the Courant-Friedrichs-Lewy condition. Different fixed time steps were chosen to carry out a time step convergence study. In Table 4, the errors are relative to the specified wave height at inlet (0.142 m, model scale) or the numerical results with the smallest time step. To limit computational effort while obtaining sufficient accuracy, a fixed time step (0.001414 s, model scale) is used in the rest of this work.

The Richardson extrapolation with the standard power-law error estimator [36] is used to obtain the wave loads at the limit of infinite temporal and spatial resolution. The resulting apparent order of convergence is 2. The discretization uncertainty is defined as the estimated discretization error multiplied to a suitable safety factor (1.25 following the recommendation from Eça and Hoekstra [37]). The total uncertainty is given by combining the temporal and spatial discretization uncertainties in the root-sum-of-squares fashion, shown in the last column of Table 6.
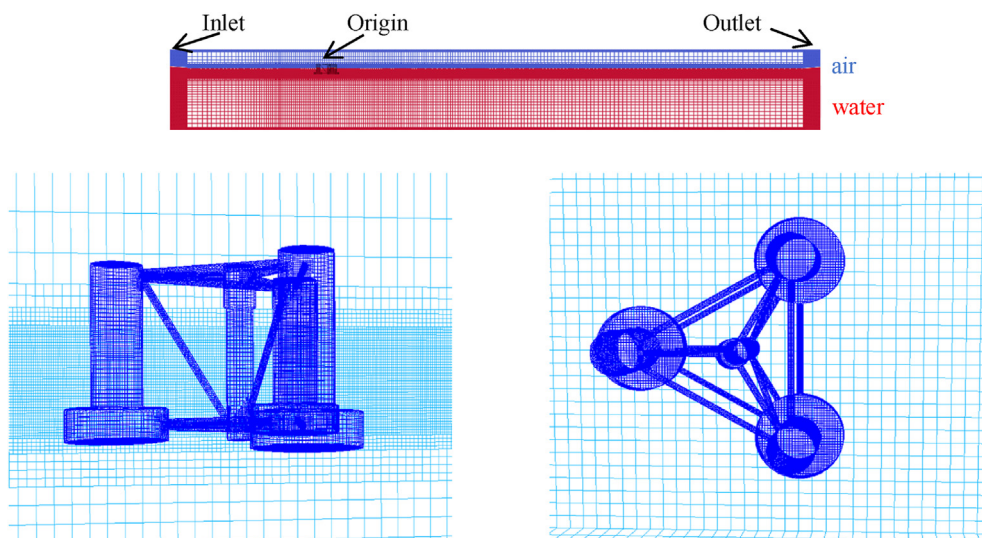
Fig. 3. The computational domain (top) and mesh around the floater (bottom) in CFD simulations.

Table 3
Mesh convergence study (model scale, same time step). Errors in the forces/moments are computed with reference to the Level 4 results.

Spatial discretization	Calculated wave height at origin (m)	Error	Calculated surge force (N)	Error	Calculated heave force (N)	Error	Calculated pitch moment (Nm)	Error
Level 2 ($\approx$ H/5)	0.1413	0.493%	223.08	0.52%	61.40	9.44%	68.11	3.41%
Level 3 ($\approx$ H/10)	0.1416	0.282%	224.20	0.13%	64.07	5.50%	68.41	2.97%
Level 4 ($\approx$ H/20)	0.1417	0.211%	224.25	–	67.80	–	70.52	–
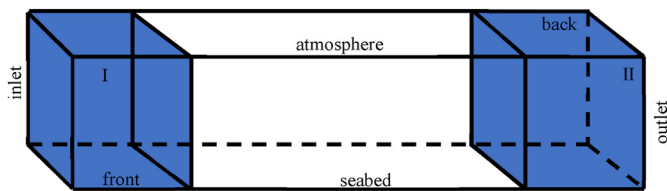
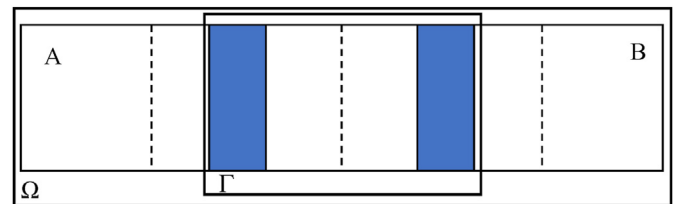**Fig. 4.** Schematic representation of computational domain.

Fig. 5. Schematic representation of the potential solver domain Ω, and waveFoam solver domain. Γ

3.1.6. Coupling of Navier-Stokes and potential flow solver

For the irregular wave case, an efficient domain decomposition strategy is implemented. As illustrated in Fig. 5, the smaller CFD domain Γ where the Navier-Stokes/VOF equations are solved is coupled with a larger potential flow domain Ω, where a larger mesh size can be applied. The coupling zones are the relaxation zones in the waves2Foam toolbox. The coupling strategy is based on one-way coupling, where the information only propagates from outer domain to inner domain. No target solution for the air velocity is provided in the potential flow solver, and zero air velocity is strongly imposed on the coupling domain boundaries. Domain A and B are the relaxation zones in the potential flow solver. More details regarding the coupling method can be found in the work of Paulsen et al. [25].

3.2. Potential flow theory model

In addition to the CFD model, a numerical model based on potential flow theory has been built using the software SIMA (SIMO-RIFLEX) [38,39], developed by SINTEF Ocean and widely used in the analyses of numerous types of offshore platforms and wind turbines.

In present simulations, only the stationary semi-submersible floater is modelled. First order potential flow forces, such as the wave excitation force, and second-order sum-frequency and difference-frequency wave force transfer functions (QTFs) are estimated based on a potential flow solution (WAMIT [40]) and subsequently input to SIMA. In addition, viscous effects are considered by applying drag forces from Morison's equation to the columns and cross braces. A constant drag coefficient in the normal direction (0.774, based on towing tests [20]) is applied for each part of the floater. The axial drag force on the heave plate is calculated based on Equation (9). D is the diameter of the heave plate. U is the water particle velocity along the axial direction. Here, we use $C_{da} = 2.48$ based on previous comparisons of a similar engineering tool with experimental data from the DeepCwind test campaign [41].

$$F_{DA} = \frac{1}{2}\rho C_{da}\frac{\pi D^2}{4}U|U| \tag{9}$$

In the SIMA simulations, different force contributions are investigated, as summarized in Table 5. For simulations labelled 'SIMA', the experimentally measured wave elevation is used as input, while simulations indicated as 'Linear' use a fully linear regular wave (same period and height as experimental wave). When the experimentally measured wave elevation is used as input, all components are treated as linear, and all components are assumed to travel in the positive x-direction.

4. Results

In this section, nonlinear wave diffraction loads on a semi-submersible FWT are studied in detail, and all the results are shown at full scale. Considering symmetry, nonlinear wave loads on the starboard column are presented for only one of the trailing columns (starboard, see Fig. 1).

4.1. Regular wave

In the examination of regular wave results, wave amplitudes and loads are extracted from five out of 20 steady-state wave cycles. First, second and third harmonic components are obtained by filtering the signals to keep components around 1ω, 2ω and 3ω, where ω is the wave frequency. The amplitude is the average value over the five wave cycles and the phase represents the initial phase. The uncertainty in the measured wave elevation is estimated as 0.03 m full scale [42].

Numerically calculated waves at the center of floater are compared against the experimental results in Fig. 6, which shows a good agreement except for a fully linear regular wave (SIMA + Linear). The small difference between SIMA and

Table 4
Time step convergence study (model scale, Level 3 spatial discretization). Errors in forces/moments are computed with reference to the result for the smallest time step.

Temporal discretization (s)	Calculated wave height at origin (m)	Error	Calculated surge force (N)	Error	Calculated heave force (N)	Error	Calculated pitch moment (Nm)	Error
0.00707	0.1390	2.11%	219.45	2.43%	61.17	9.54%	64.40	7.80%
0.002828	0.1410	0.70%	223.05	0.83%	63.23	6.49%	67.64	3.16%
0.001414	0.1416	0.28%	224.20	0.32%	64.07	5.25%	68.41	2.06%
0.000707	0.1418	0.14%	224.92	–	67.62	–	69.85	–

Table 5
Overview of different settings in SIMA.

Label	Theory
SIMA1/Linear1	Only linear potential flow theory
SIMA2/Linear2	SIMA1/Linear1 with sum-frequency (for regular wave case)/difference frequency (for irregular wave case) wave force transfer function (QTF)
SIMA3/Linear3	SIMA2/Linear2 with integration of Morison drag force to mean free surface
SIMA4/Linear4	SIMA2/Linear2 with integration of Morison drag force to the undisturbed linear free surface
SIMA5/Linear5	SIMA4/Linear4 with consideration of axial drag force on the heave plates

experiment is caused by a low-pass filter used in SIMA. This filtering also results in the non-dimensional wave amplitude of the fully linear regular wave deviating slightly from unity. Additionally, the numerical damping is negligible in the CFD simulations. Moreover, the numerical wave with laminar flow (L.F) has a smaller variation in the wave height over different cycles, with a standard deviation of 0.0018 m, compared to 0.0047 m for the turbulent flow (T.F) model and 0.0067 m for the experiment. Compared to the experimental results, the CFD-generated waves can capture the first harmonic wave elevation but have less wave energy at twice the wave frequency. The reduction in second harmonic wave elevation with turbulent flow is due to viscous damping.

4.1.1. Upright condition

The surge forces on the upright floater are presented in Fig. 7. SIMA5 is not shown because the axial drag force on the heave plate

(z direction) does not contribute to the surge force (x direction) on the upright floater. The amplitude and phase for the total and first harmonic surge force are predicted very well (within 2.5%) by all numerical simulations. For higher order surge forces, CFD results show a similar phase as the experiment. The simulations with laminar flow overpredict the second harmonic surge force and underpredict the third harmonic, while CFD results with turbulent flow are closer to the experimental measurements. Compared to the laminar flow, the turbulent flow has a lower pressure drag contribution and a higher friction drag contribution. In SIMA, the viscous effects are considered through the water particle velocity. Because the mass loads, proportional to water particle acceleration, dominate for the considered structure and wave, the phase difference between water particle acceleration and velocity leads to a phase-lead in the SIMA 4 surge force compared to the experiment. Furthermore, SIMA 4 underpredicts the third harmonic surge force,
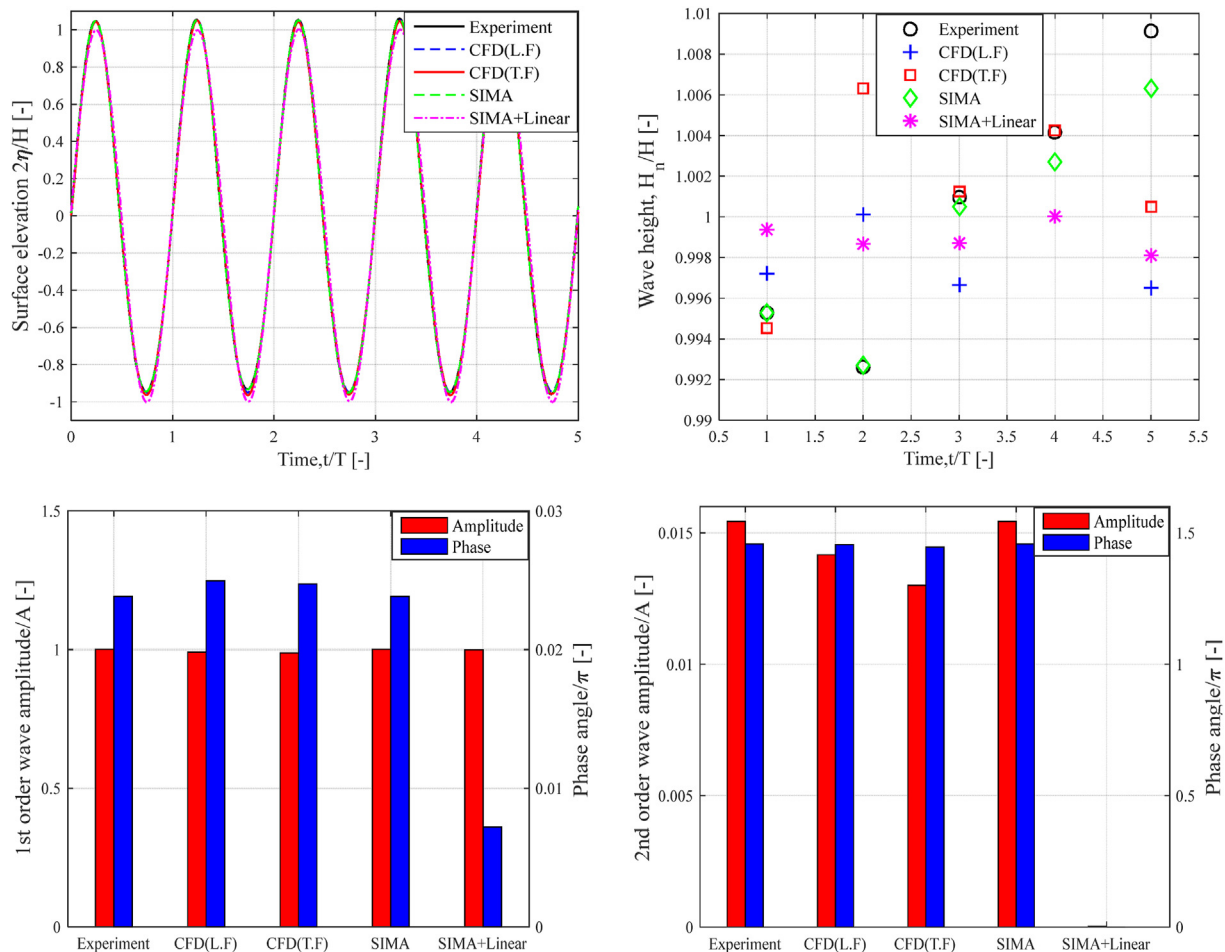
Fig. 6. Comparisons of the free surface elevation for the regular wave. H and A are the specified wave height and wave amplitude while H_n is the measured or simulated wave height. Top left: time series of total surface elevation, top right: total wave height over time, bottom left: average first harmonic wave amplitude, bottom right: average second harmonic wave amplitude.
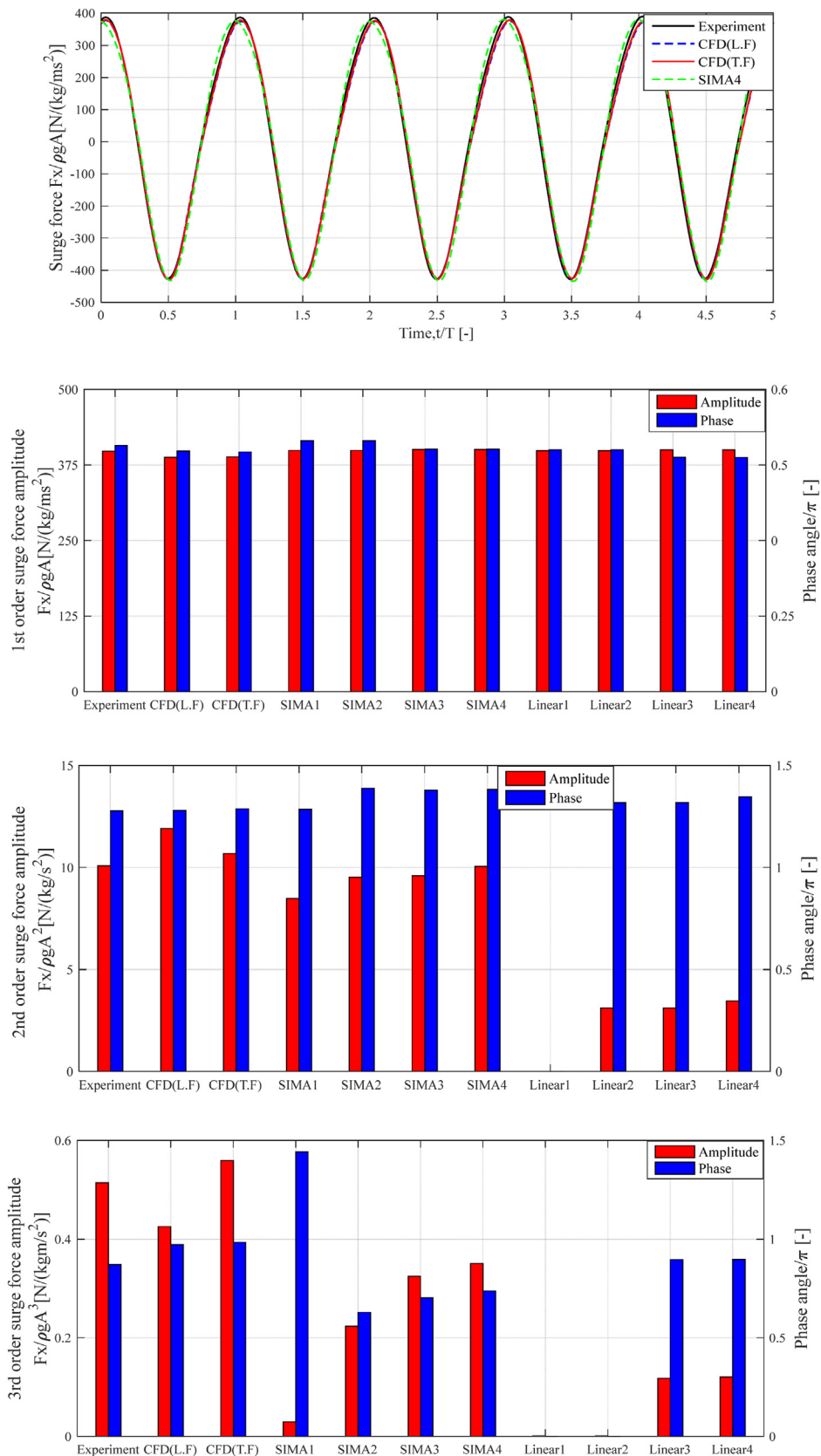
Fig. 7. Comparisons of surge force (CFD, SIMA and experiment) under upright condition for the regular wave (from top to bottom: time series of total surge force, amplitude and phase of first harmonic, second harmonic and third harmonic surge force).

and there is a phase difference between SIMA and experiment for higher order results, which can be explained by decomposing the higher order surge forces.

Even though the experimental wave is treated as a linear wave in SIMA, the measurements contain higher order components compared to the fully linear regular wave. A comparison of SIMA 1–4 and the 'Linear' results shows that the nonlinearity in the wave elevation dominates the higher order surge forces. Additionally, the sum-frequency QTF and integration of the drag force to the undisturbed linear free surface contribute to the second harmonic surge force. In the SIMA 2–4 models, the combination of high-frequency wave components and the sum-frequency QTF lead to a third harmonic surge force. The nonlinear drag force also contributes to the third harmonic surge force. The 'Linear' results show good phase agreement compared to the experiment. For the SIMA 1–4 results, the treatment of nonlinear components of the incoming wave leads to phase discrepancy. The applied constant normal drag coefficient in SIMA may also contribute to amplitude differences in the higher order surge forces.

The heave forces on the upright floater are compared in Fig. 8. SIMA 1–4 and CFD with laminar flow underestimate the amplitude by 15%, while CFD with turbulent flow agrees well with the experiment (within 5.8%). Turbulent flow increases the first and third harmonic heave force but reduces the second harmonic. Flow separation around the edge occurs due to the geometric singularity and leads to a larger vertical drag force. However, the RANS model used in this paper may not simulate this effect correctly, and overpredicts the third harmonic heave force by over 50%. Like the surge force, the CFD model has a similar phase as the experiments, while SIMA 1–4 deviates for all harmonics.

When axial drag forces on the heave plates are not included (SIMA 1–4), most of the heave excitation comes from potential flow theory, and the first and third harmonic heave forces are underpredicted, while the second harmonic is overpredicted. Additionally, the normal drag force on the cross braces slightly increases the third harmonic heave force (SIMA 2 vs SIMA 3). From the comparisons between SIMA 1–4 and the 'Linear' results, nonlinear incoming wave also contributes to the higher order heave forces. Furthermore, the phase of the higher order heave force also deviates from the experiments in the 'Linear' results.

The axial drag force (SIMA 5 and Linear 5) increases the first and third harmonic heave force, while the integration of the drag force to the linear free surface also increases the second harmonic. SIMA 5 predicts the phase better than SIMA 1–4, but still differs from the experimental results in the higher order results. This suggests that potential flow theory and Morison-type drag with a tuned axial drag coefficient can predict the amplitude of the heave force very well, without really capturing the physics, as evidenced by the difference in the phase.

Fig. 9 compares the numerically estimated pitch moment against the measured result. All numerical models underpredict the first harmonic amplitudes (from 1.6% for SIMA 5–7.8% for CFD with turbulent flow) but have similar phase as the experimental data. The discrepancy in amplitude may be caused by the underprediction of the heave forces. In the CFD simulation, the second harmonic pitch moment performs similarly as the surge and heave forces, but for the third harmonic, the model with turbulent flow underestimates the amplitude by 28%. The SIMA 1–4 simulations underpredict higher order amplitudes and differ in phase from the experimental results. The phase difference also exists when the axial drag force on the heave plate is included (SIMA 5).

For the second harmonic pitch moment, a comparison of the SIMA and Linear 1–4 models shows that nonlinearity in the incoming wave is important (linear potential flow theory dominates). Furthermore, the sum-frequency QTF reduces the amplitude

(SIMA 2 vs. SIMA 1). The normal drag force has no obvious effect on the second harmonic pitch moment.

For the third harmonic, the moment induced by the sum-frequency QTF is more important than other contributions for SIMA 1–4. Meanwhile, by comparing SIMA 3–4 and 'Linear' results, the third order contributions from normal drag forces due to high-frequency wave components reduce the amplitude. The axial drag force (SIMA 5 and Linear 5) mainly contributes to the third harmonic pitch moment and has no significant effect on the first or second harmonic. In conclusion, the first and second harmonic pitch moments in SIMA are mainly from potential flow theory and only the axial drag forces on the heave plates have a significant effect on the third harmonic.

The differences between measured wave loads in the experiment and calculated wave loads in the CFD with turbulence model are compared with the estimated uncertainty in Table 6. As shown, the differences for the total wave loads are within the range of sum of uncertainties in experiment and numerical results. Both the differences and uncertainties in higher order components may be larger, however.

The experiments do not measure surge forces on individual columns, but this comparison can be carried out numerically, shown in Fig. 10 and Fig. 11. Here, the sum-frequency QTF is not included in SIMA. Therefore, wave nonlinearity is important for the first and second harmonic surge forces, while the drag force is dominant in third harmonic in these results.

For the first harmonic surge force, SIMA and CFD are in better agreement for the upper column (within 2.4%) than for the heave plate (within 10.2%). In the CFD model, the intersections between heave plates and cross braces are modelled, which reduces the heave plate flank area where the pressures are integrated by 1.33%. The SIMA model considers the heave plates as closed cylinders. As with the total force, due to the constant drag coefficient in SIMA, there is a large difference in the amplitude and phase of higher harmonic surge forces between SIMA and CFD.

For the CFD results, except for the higher order surge force on the upper column of the upstream column (Fx2), the surge forces have similar phase for both laminar and turbulent flow in each harmonic. According to the KC number in Table 2 and results from other researchers [43], a pair of weak vortices is formed in the wake of upper column of upstream column which laminar flow model cannot simulate. In Fig. 10, the flattened peak value of the surge force on the main column (Fx1) is due to the geometry: the top of main column has larger diameter which leads to a ledge (see left part of Fig. 1). This ledge leads to the large difference in the third harmonic surge force of main column between laminar and turbulent flow model. This phenomenon is not modelled in SIMA.

For both the upstream and starboard column, although the diameter of the heave plate is twice that of the upper column, the surge force on the upper column is larger because the water particle acceleration decreases as one moves downward. To better understand these results, the surge forces on each column under fully linear regular waves with different wave periods and the same wave steepness were estimated using the SIMA 4 model, shown in Fig. 12. Based on the previous analysis (Fig. 7), the main difference between the total and first order amplitude (right part of Fig. 12) is due to the third harmonic drag force. The total surge forces on the upper column (Fx2 and Fx4) are also larger than the forces on the heave plate (Fx3 and Fx5), and the discrepancy increases for shorter waves. Comparisons among the higher order surge forces lead to the same conclusions, but the discrepancy depends on frequency.

Comparing the forces on components of the upstream column and starboard column in the CFD simulations (Fig. 11), the amplitude of higher order surge forces on the starboard column is larger than those on the upstream column. The same can be observed in
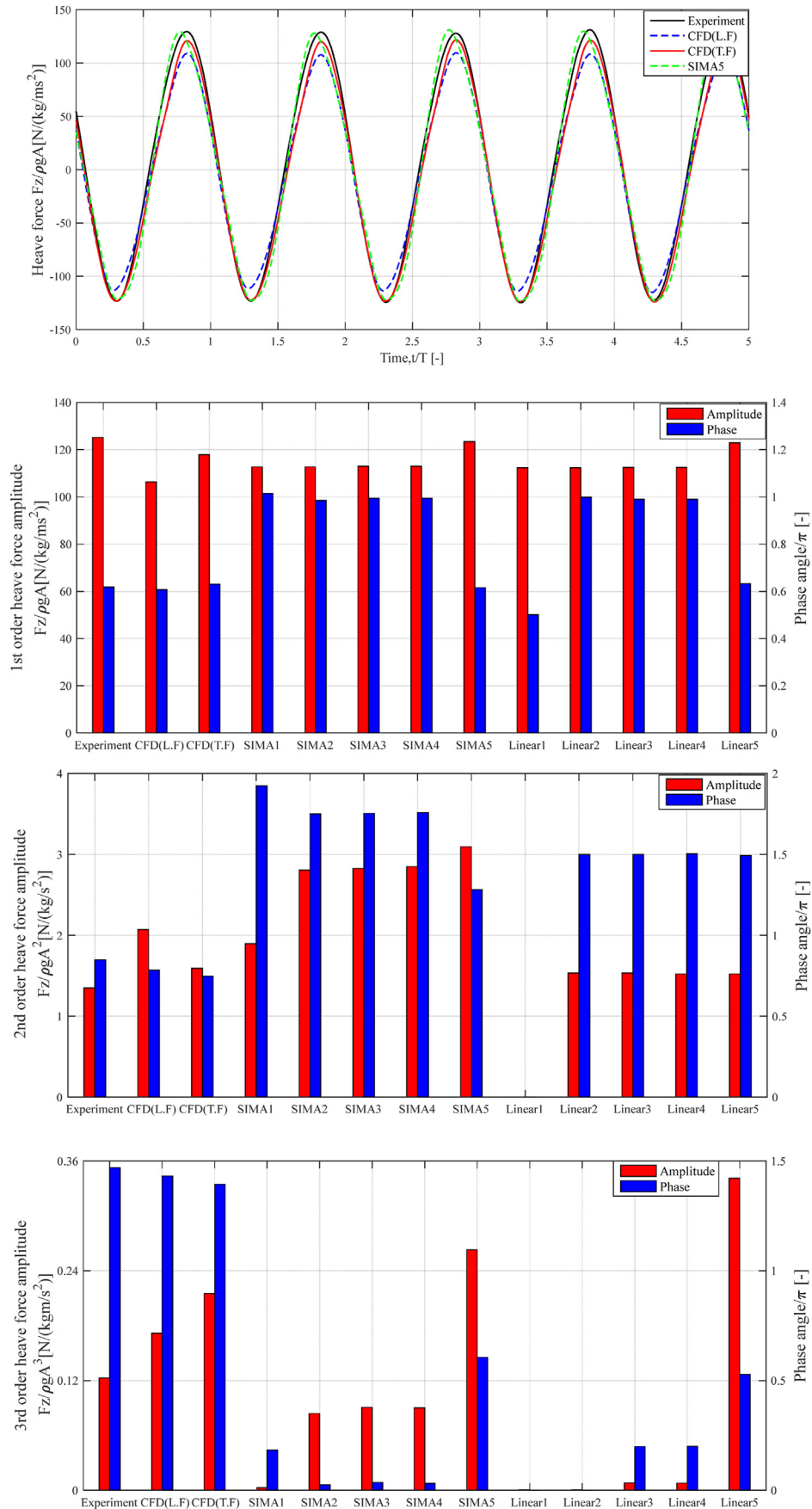
Fig. 8. Comparisons of heave force (CFD, SIMA and experiment) under upright condition for the regular wave (from top to bottom: time series of total heave force, amplitude and phase of first harmonic, second harmonic and third harmonic heave force).
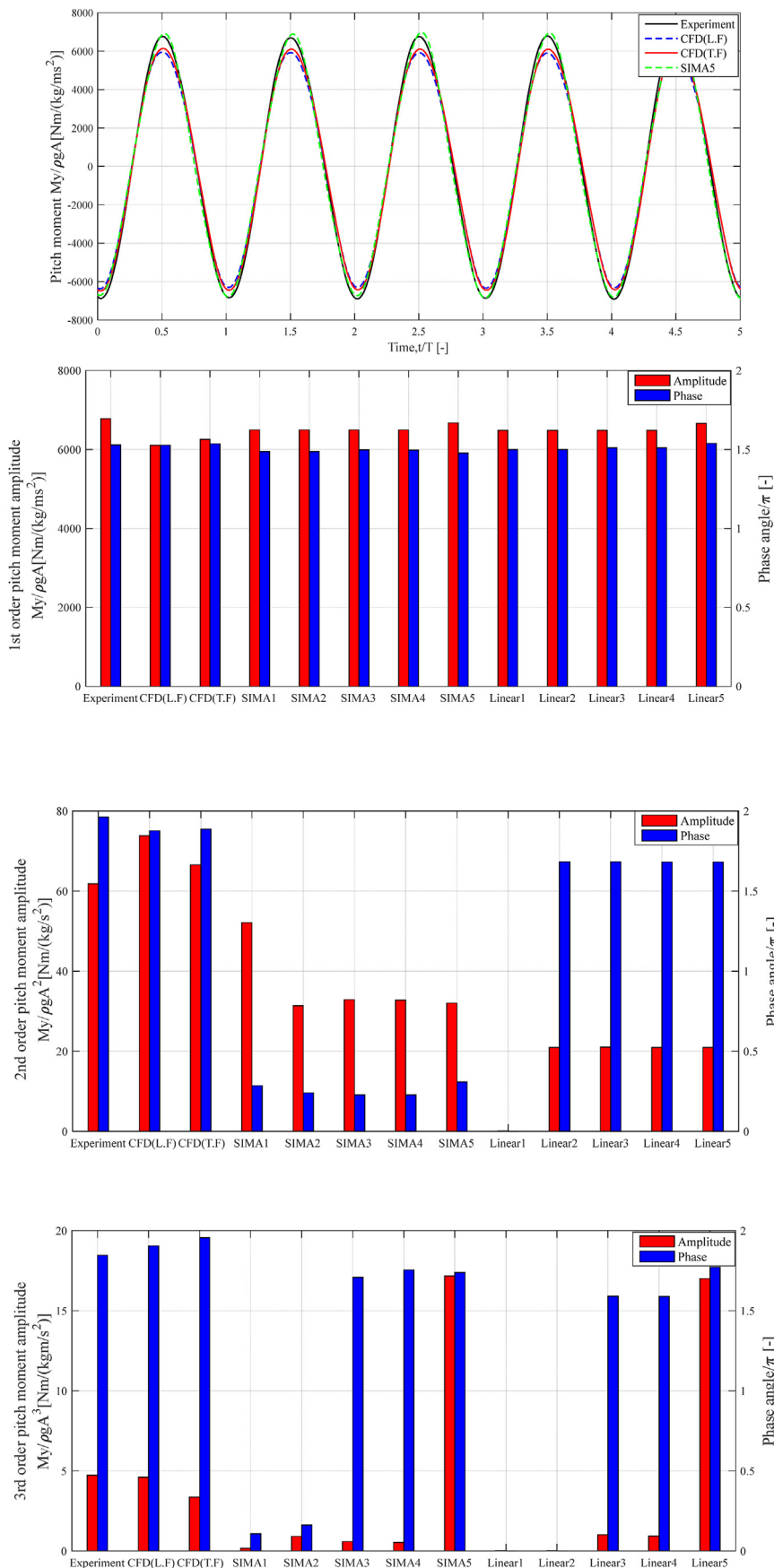
Fig. 9. Comparisons of pitch moment (CFD, SIMA and experiment) under upright condition for the regular wave (from top to bottom: time series of total pitch moment, amplitude and phase of first harmonic, second harmonic and third harmonic pitch moment).

Table 6
Comparisons of differences between experiments and CFD simulations and uncertainties for the total wave loads under upright condition.

	Difference between experiment and CFD with turbulence model	Uncertainty in experiment	Uncertainty in numerical results
Surge force	2.5%	2%	0.60%
Heave force	5.8%	2%	14.28%
Pitch moment	7.8%	5%	5.71%

the first and third order surge forces in SIMA simulations (Fig. 11) while the opposite is seen in the second order surge force. The results under different wave periods (Fig. 12) show that the surge force comparison between the starboard and upstream column depends on frequency.

4.1.2. Trimmed condition

Considering the existence of a mean pitch angle for the wind turbine during operation, nonlinear wave diffraction loads on a $5°$ trimmed floater are studied in this section. The floater is rotated $5°$ clockwise around Point A shown in Fig. 1. No corresponding experimental data are available. Only results from CFD with turbulent flow and the SIMA model are shown in this section. Furthermore, we focus on the integrated wave loads on the complete floater. Surge force (along x axis), heave force (along z axis) and pitch moment (around y axis) are calculated in the same global coordinate system as the upright condition which is shown in Fig. 1. The amplitudes of load responses divided by the xth ($x = 1,2,3$) power of the displaced submerged volume V ($\times 10^4$ m^3) are also compared to eliminate the effect of changed submerged volume, which is denoted as 'Amplitude/V^x' in Figs. 13—15.

The surge forces under upright and trimmed conditions are presented in Fig. 13. The first harmonic surge force under trimmed condition increases (4.8% for CFD and 2.4% for SIMA) compared to the upright condition. After rotating the floater, a larger portion of the columns are submerged, but the water particle acceleration at the same position of columns decreases. Hence, considering the changed volume, the first harmonic surge force under trimmed condition decreases (5.2% for CFD and 4.7% for SIMA). The higher order results generally decrease, especially when considering the changed volume.

As shown by 'SIMA5+$5°$' in Fig. 13, the axial drag force increases the first harmonic surge force by 3.2% and decreases the third harmonic by 4.2% (SIMA5 has the same value as SIMA4 under upright condition). For the trimmed floater, the axial drag forces on the heave plates have a component along x direction. The water particle velocity along the column axis is the resultant velocity of the vertical and horizontal water particle velocity, which have a phase difference. Hence, the contribution of this additional drag force depends on the phase.

The heave forces under upright and trimmed position are compared in Fig. 14. All harmonics of the heave force decrease after rotating the floater except for a slightly increased second harmonic CFD result. Considering the changed volume, all harmonics decrease. The increased heave force on the upper column cannot compensate for the loss of heave force on the heave plate. In the SIMA 4 model without axial drag force, this decreasing heave force relates to the change of immersed geometry. By comparing 'SIMA4+$5°$' and 'SIMA5+$5°$', the axial drag force increases the heave force in each harmonic, especially at the third harmonic (around 200%). Furthermore, the axial drag force (SIMA5+$5°$) is mainly calculated based on the vertical water particle velocity, which leads to a phase shift for each harmonic heave force compared to the 'SIMA4+$5°$'. Normalizing by submerged volume, there is almost no change in the SIMA5 results due to trim.

The comparisons of numerically estimated pitch moment are

shown in Fig. 15. For the CFD simulations, except for the deceasing second harmonic results (15.3%), there is an increasing pitch moment (within 9.3%) on the trimmed floater. All harmonic pitch moments in SIMA 4 model increase (around 7% for the first harmonic, 60% for the second harmonic, 100% for the third harmonic) in the trimmed condition due to the changed results from linear potential flow theory. The axial drag force increases the third harmonic pitch moment (14 times larger) and decreases second harmonic pitch moment (11.2%) by comparing 'SIMA4+$5°$' and 'SIMA5+$5°$'. However, the total pitch moment increases by 1%. Similar to the heave force, when dividing by submerged volume, there is almost no change in the SIMA5 results due to trim.

4.2. Irregular wave

An irregular wave state ($H_s = 7.1$ m and $T_p = 12.1$ s) is considered to investigate the wave loads near natural periods of rigid body motion. In the CFD model, as the wave maker motion in the experiment is not available, the measured irregular wave at the center of body is used to generate a time series of wave elevation at the wave maker as an input signal at the inlet of potential flow domain, following the procedure shown by Bachynski et al. [44]. The outlet boundary of the potential flow domain is defined by setting a constant current with zero velocity. The spatial discretization in the CFD domain is the same as in the regular wave case. The cell size in the potential flow domain is 10 times larger. The center of the two computational domains is co-located with the center of the floater. Due to excessive numerical damping for wave generation with a turbulence model, the CFD laminar flow model is used. The wave in SIMA is obtained by filtering the measured wave elevation at the origin with a 0.025 Hz cut-off frequency. For the SIMA 2 model, the sum-frequency QTF is replaced with the difference-frequency QTF. In this section, the power spectral density (PSD) of responses is calculated based on the time series from 1200s to 4800s and we only focus on low frequencies. In the wave-frequency region, the agreement is very good among all results, and is not shown.

Experimental and numerical time series of 20 wave cycles extracted from 1-h simulations and the wave power spectra (in log scale) for the full hour are compared in Fig. 16. Although there is a difference in the low-frequency domain, the values are quite small compared to the ones in the wave-frequency domain where good agreement occurs and have no significant effect on the obtained wave energy. Hence, to be fair, CFD can reproduce the wave elevation very well. Based on the difference between wave power spectrum at inlet and center of CFD domain, most of numerical damping in the CFD domain occurs in the low-frequency domain. The effect of the cut-off frequency (0.025 Hz) is visible in the SIMA simulations.

The numerically estimated low-frequency surge force power spectra are compared against experimental results in Fig. 17 (left). SIMA underestimates the low-frequency surge forces, and by 26.6% at surge natural frequency. CFD also underpredicts the surge forces by 16.2% at the surge natural frequency. On the other hand, CFD results have more significant wave energy (within 20%) at low frequencies.
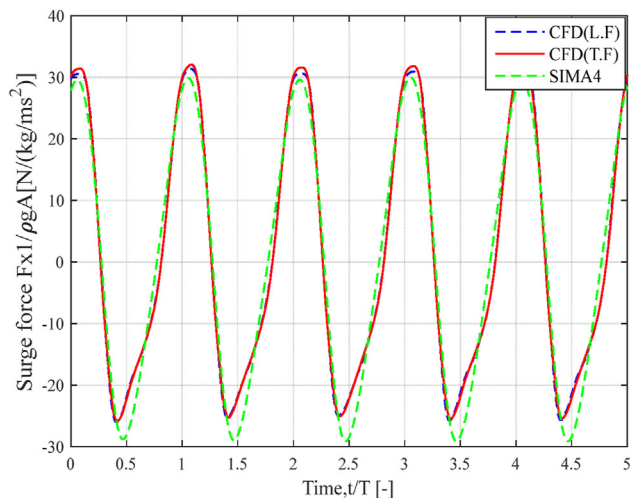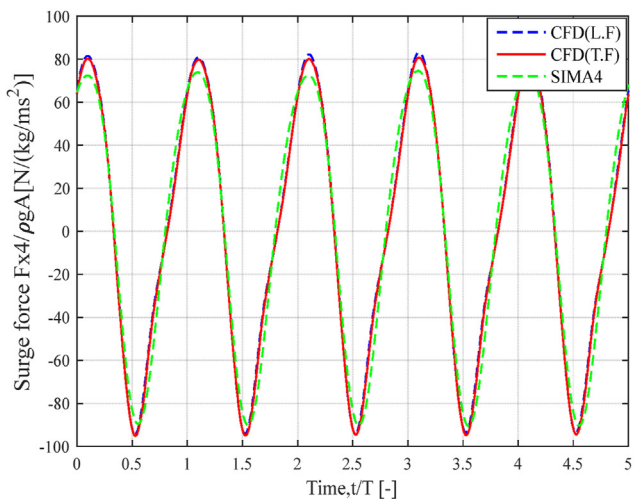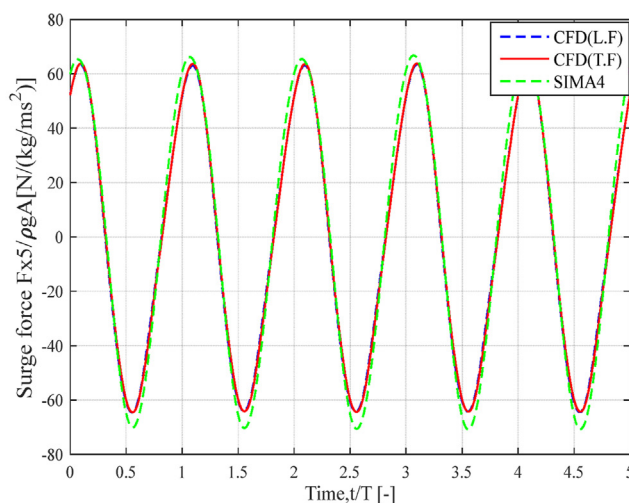
a) main column (Fx1)
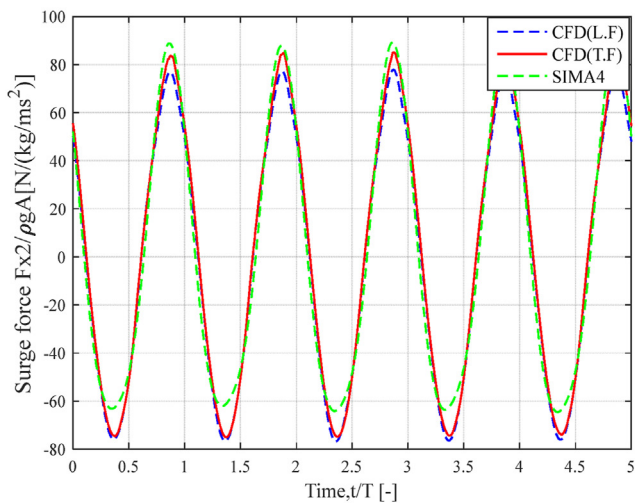
b) upper column of upstream column (Fx2)
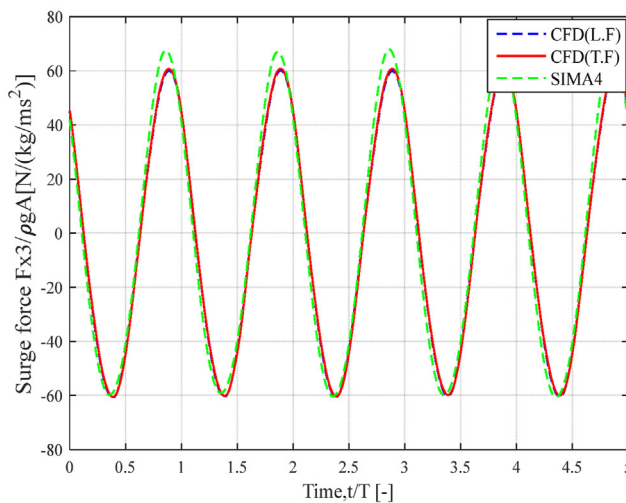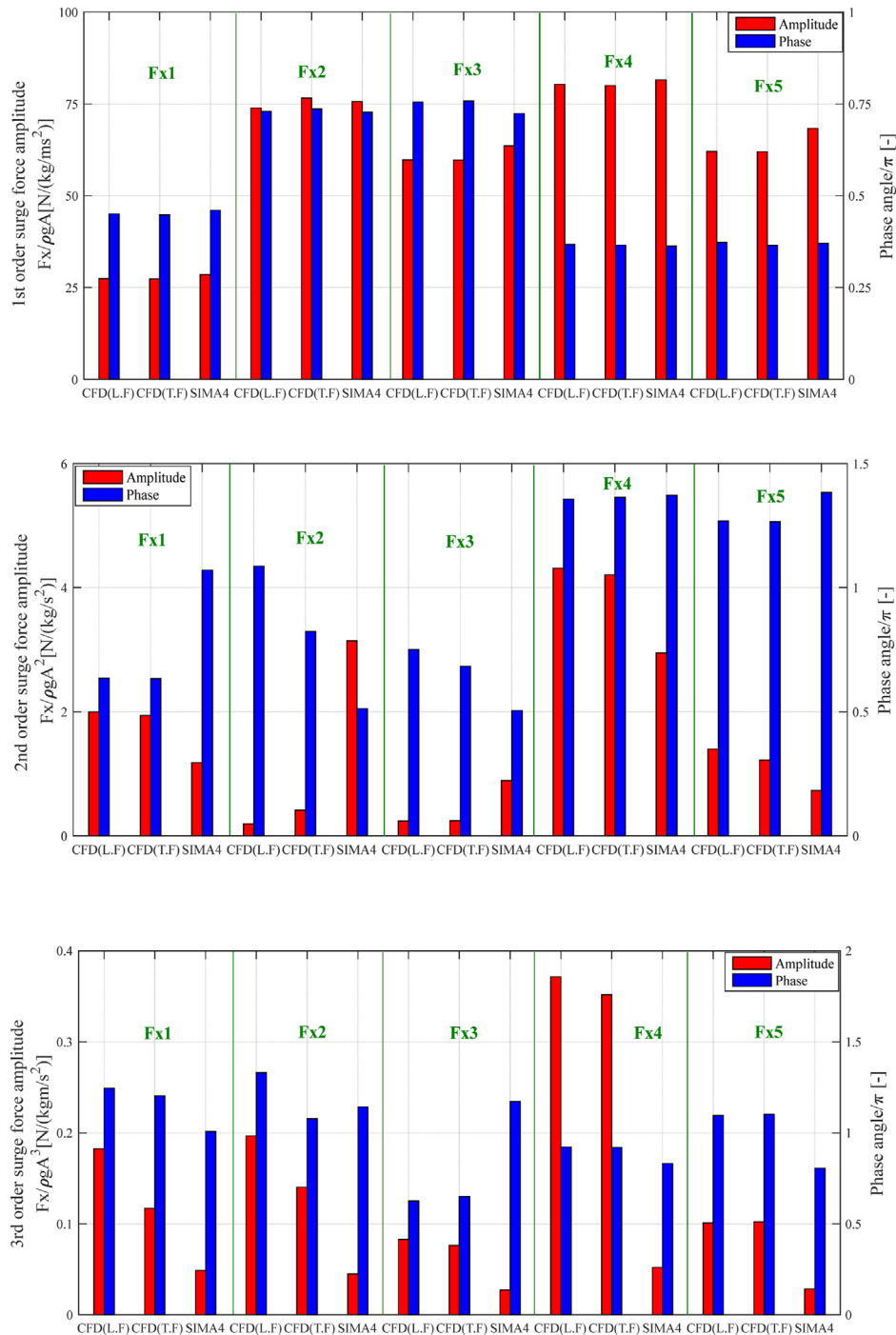

c) heave plate of upstream column (Fx3)

d) upper column of starboard column (Fx4)

e) heave plate of starboard column (Fx5)

Fig. 10. Comparisons of time series of total surge forces on the individual columns of the floater (CFD and SIMA) under upright condition for regular wave.

Fig. 11. Comparisons of first, second and third harmonic surge forces on the individual columns of the floater (CFD and SIMA) under upright condition for the regular wave (from top to bottom: amplitude and phase of first, second and third harmonic surge force on different columns, Fx1: main column, Fx2: upper column of upstream column, Fx3: heave plate of upstream column, Fx4: upper column of starboard column, Fx5: heave plate of starboard column. See Fig. 1 for the definitions of columns).

Fig. 17 (right) presents the low-frequency surge force spectra considering different force contributions in SIMA. All of the components of the measured irregular wave are treated linearly in SIMA. The surge natural frequency is below the cut-off frequency, so there is no significant linear wave excitation (SIMA 1) at surge natural frequency. The difference-frequency QTF (SIMA 2) has a slight influence on the low-frequency surge force. The surge force at surge natural frequency is mainly from integration of the Morison drag force to the linear free surface (SIMA 4). The axial drag forces

on the heave plates have no effect on the low-frequency surge force (SIMA 5 vs SIMA 4).

The heave force spectra are compared in Fig. 18 (left). SIMA underestimates the low-frequency heave forces, and by 20.5% at the heave natural frequency. The CFD model shows better predictions of heave forces, however, there is also significantly less wave energy (18%) at the heave natural frequency in the CFD model. It is important to note that the laminar flow model used in CFD simulation cannot correctly capture the flow around the heave plate. A
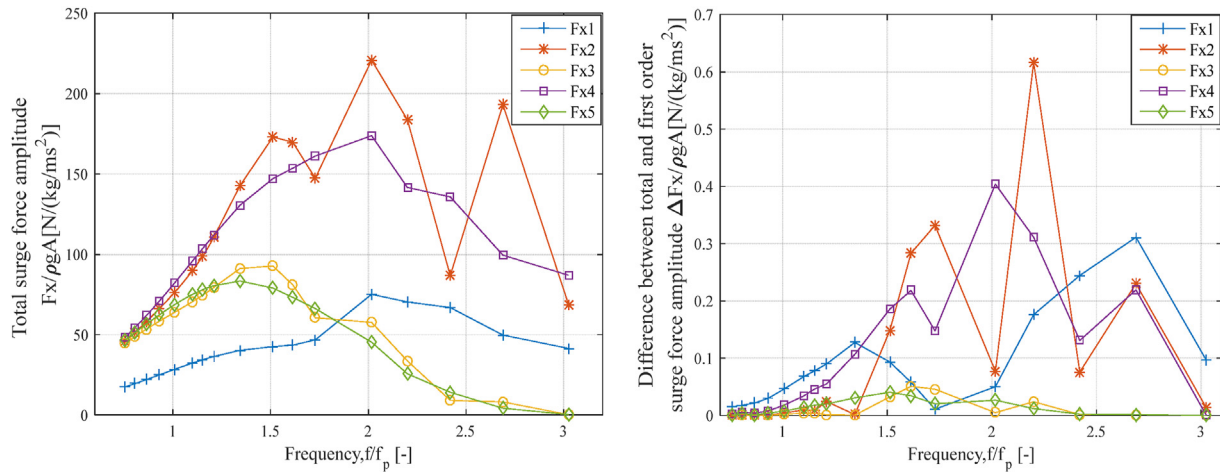
Fig. 12. Comparisons of total (left) and difference between total and first order (right) surge forces on the individual columns of the floater (SIMA 4) under upright condition for a series of fully linear regular waves with different wave periods and the same wave steepness with one used in this paper. (f_p is wave frequency used in Fig. 11). Fx1: main column, Fx2: upper column of upstream column, Fx3: heave plate of upstream column, Fx4: upper column of starboard column, Fx5: heave plate of starboard column. See Fig. 1 for the definitions of columns).

large part of the heave force comes from linear potential flow theory (SIMA 1), see right part of Fig. 18. The difference-frequency QTF (SIMA 2) and the normal drag forces (SIMA 3 and 4) have minor effects on the heave force. The axial drag forces on the heave plates (SIMA 5) increase the heave force by 89.5% at the heave natural frequency.
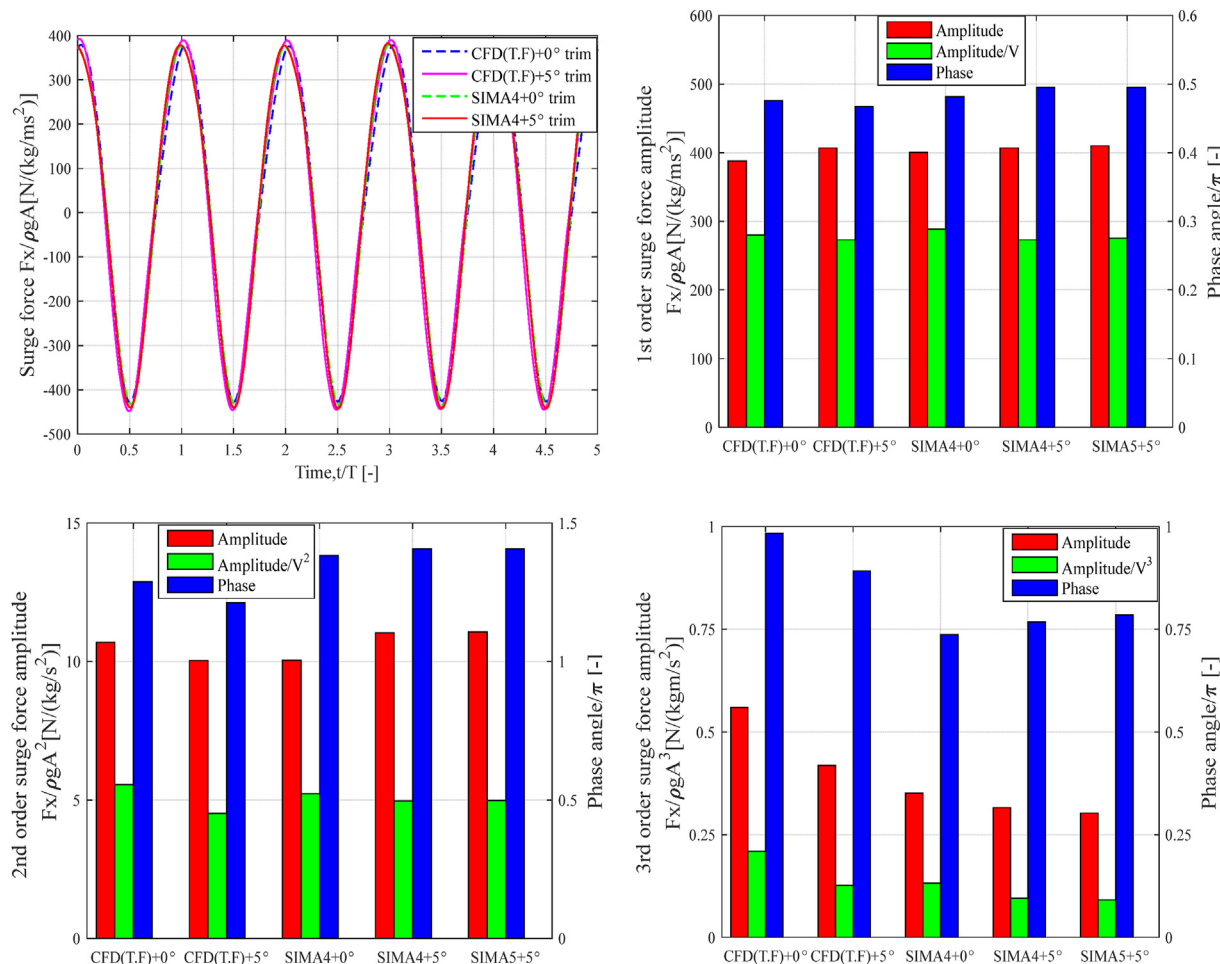
Fig. 13. Comparisons of surge forces (CFD and SIMA) under upright and trimmed condition for the regular wave (Top left: time series of total surge force, top right: amplitude and phase of first harmonic surge force, bottom left: amplitude and phase of second harmonic surge force, bottom right: amplitude and phase of third harmonic surge force).
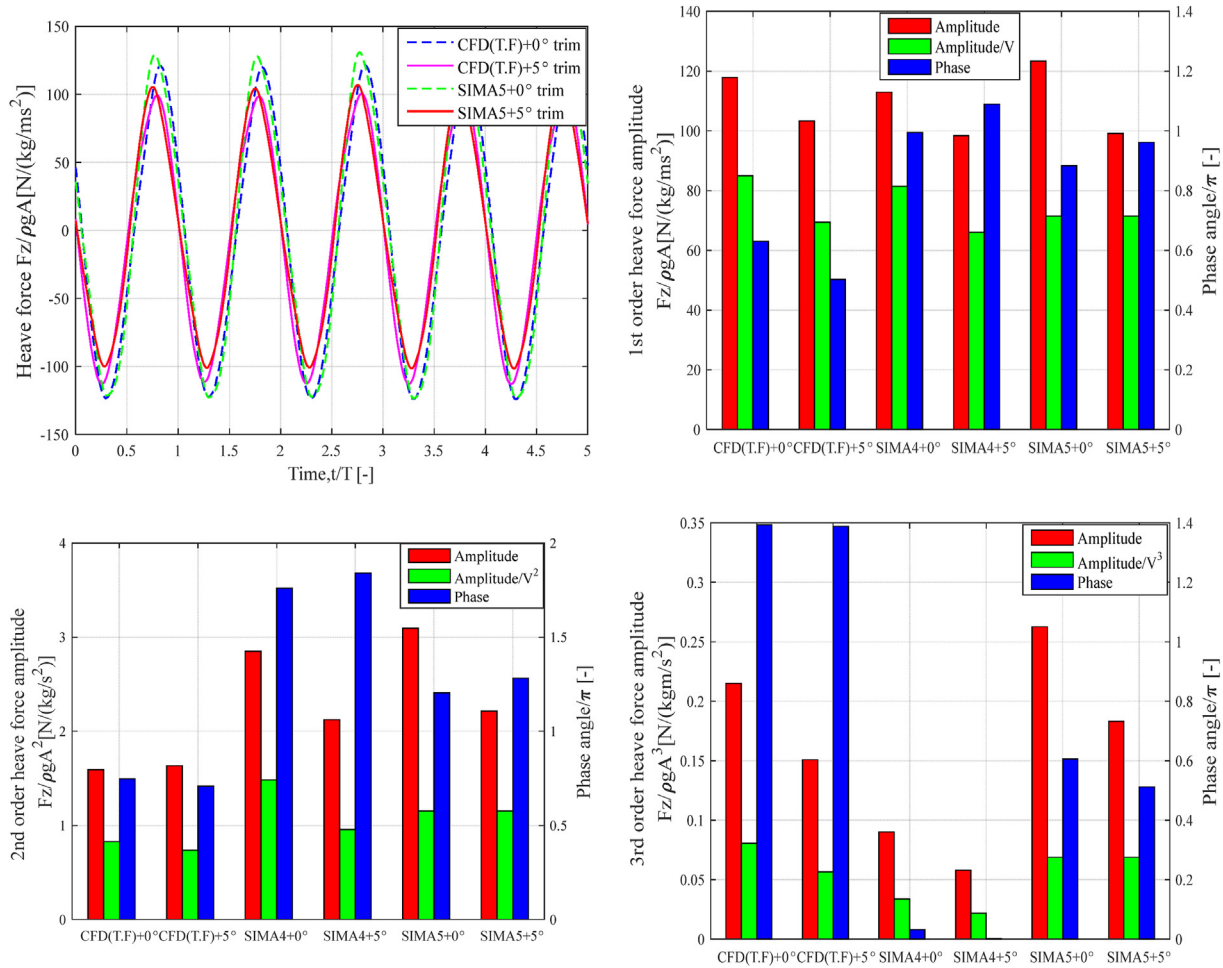
Fig. 14. Comparisons of heave forces (CFD and SIMA) under upright and trimmed condition for the regular wave (Top left: time series of total heave force, top right: amplitude and phase of first harmonic heave force, bottom left: amplitude and phase of second harmonic heave force, bottom right: amplitude and phase of third harmonic heave force).

Fig. 19 (left) compares the low-frequency pitch moment spectra. Similar to the surge and heave forces, SIMA underpredicts the pitch moment. This is consistent with previous results showing five times smaller load responses at the pitch natural frequency of a mooring FWT seen in simulations using the engineering tools compared to the experimental measurements [5]. The CFD model underpredicts the low-frequency pitch moment by about 10%. Again, this underprediction may in fact be more severe than it seems, as the CFD model includes more wave energy at low frequencies.

The comparisons of low-frequency pitch moment spectra with different force contributions in SIMA are shown in Fig. 19 (right). The pitch moment from the difference-frequency QTF (SIMA 2) is significant. In addition, the normal drag forces (SIMA 3) and integrations to the linear free surface (SIMA 4) have little effect on the pitch moment at low frequencies. The axial drag forces on the heave plates (SIMA 5) increase the moment at very low frequencies, but the results remain lower than experimental measurements.

5. Conclusions

Nonlinear wave loads are important for designing the floater and mooring system for FWTs. In this paper, nonlinear diffraction wave loads on a semi-submersible FWT are studied using two numerical approaches based on CFD and potential flow theory as well as experimental measurements.

Based on the comparisons under a regular wave, good agreement (within 10%) between numerical models and experiment is achieved for wave-frequency loads. For higher order wave loads, CFD correctly estimates the phase, and CFD with the turbulence model generally give the best results. The lower heave force and pitch moment in the laminar flow may be due to the lack of simulation for weak flow separation occurring around heave plate. SIMA (potential flow with Morison drag) has large discrepancies in prediction of phase and amplitude of higher order wave loads. The dominant higher order components in SIMA are related to treating a nonlinear wave measurement as a linear input, which leads to phase discrepancy against CFD and experimental measurements. The normal drag force of columns and cross braces in SIMA model has significant contributions to the surge force while the axial drag forces on the heave plates increase the heave force and the pitch moment. The proper drag coefficient can decrease the amplitude discrepancy in higher order loads, but a phase difference nonetheless exists in the SIMA results. This discrepancy demonstrates the limitation of potential flow theory with Morison-type drag for estimating high order diffraction wave loads.

Regarding the low-frequency wave loads on the fixed structure under an irregular wave, both CFD and SIMA underpredict the loads, but the discrepancy for CFD results is smaller. In SIMA, all of the components of the measured irregular wave are treated linearly. The difference-frequency QTF has significant contributions to the pitch moment. Normal drag forces on the columns and cross
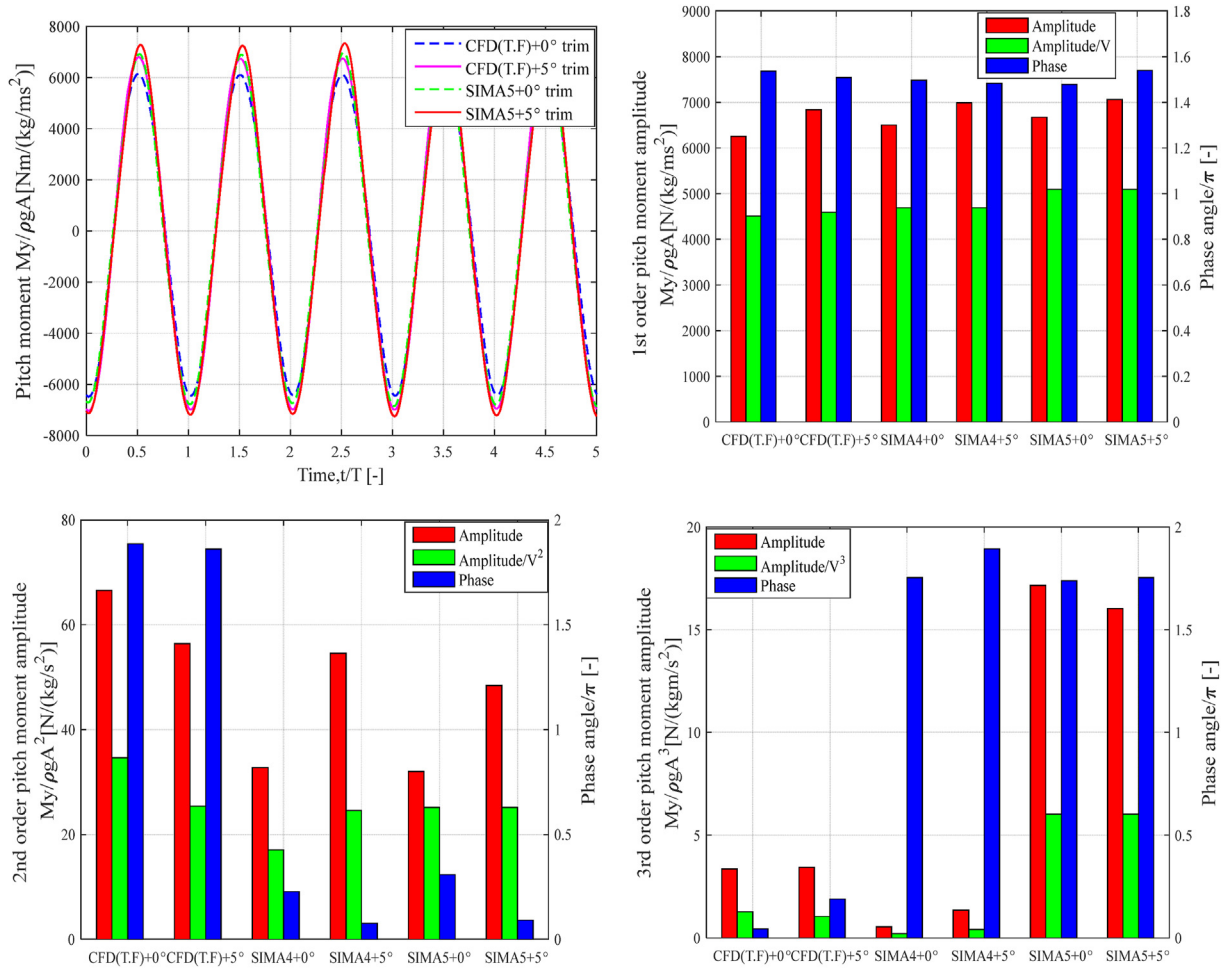
Fig. 15. Comparisons of pitch moments (CFD and SIMA) under upright and trimmed condition for the regular wave (Top left: time series of total pitch moment, top right: amplitude and phase of first harmonic pitch moment, bottom left: amplitude and phase of second harmonic pitch moment, bottom right: amplitude and phase of third harmonic pitch moment).
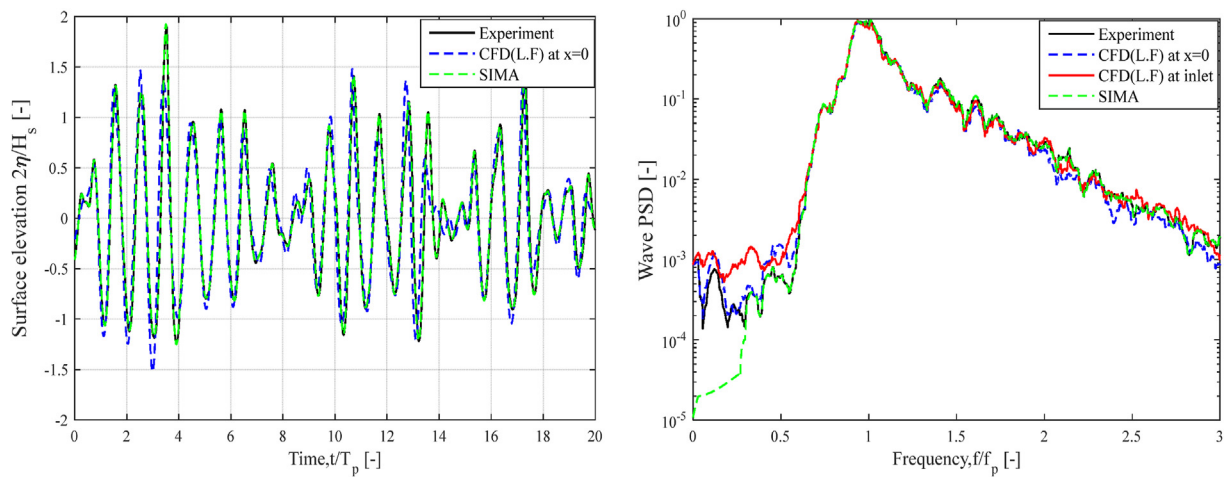

Fig. 16. Comparisons of the free surface elevation for the irregular wave (left: time series, right: wave spectra).

braces lead to an increased surge force at surge natural frequency. In addition, the axial drag forces on the heave plates largely increase the heave force at heave and pitch natural frequencies, but only contribute to the pitch moment at very low frequencies. Due to

excessive numerical damping of the wave using a turbulence model in CFD, only laminar flow was considered in the irregular waves. Further developments of hybrid methods with CFD with a turbulence model and potential flow theory models are needed.
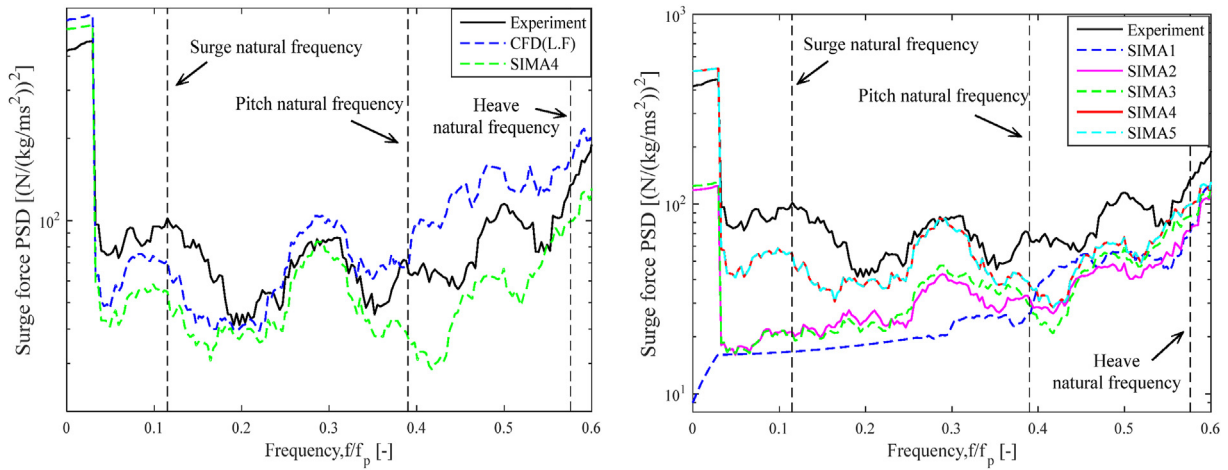
Fig. 17. Comparisons of low-frequency surge force spectra under upright position for the irregular wave (left: comparison among CFD, SIMA and experiment, right: different force contributions in SIMA).
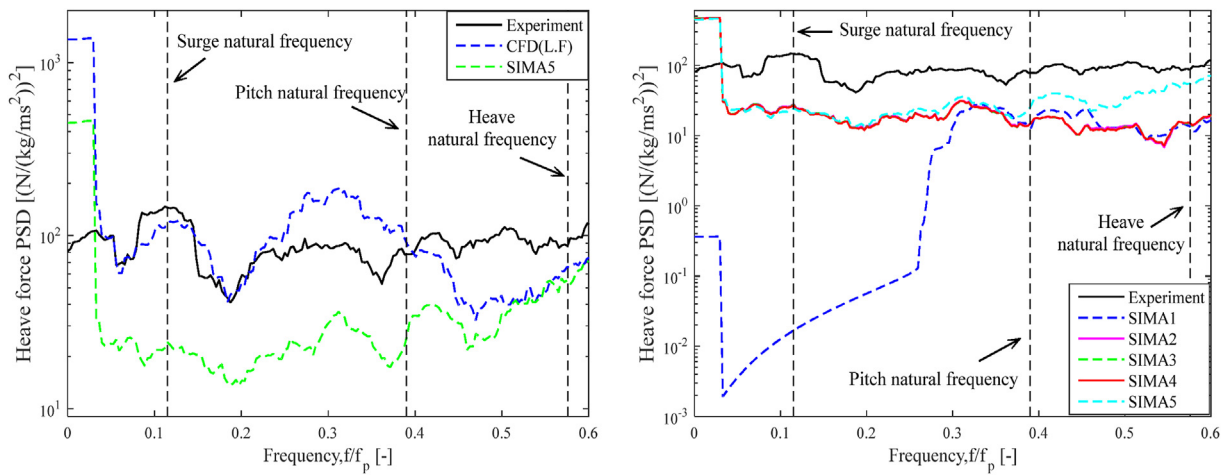

Fig. 18. Comparisons of low-frequency heave force spectra under upright position for the irregular wave (left: comparison among CFD, SIMA and experiment, right: different force contributions in SIMA).

Fig. 19. Comparisons of low-frequency pitch moment spectra under upright position for the irregular wave (left: comparison among CFD, SIMA and experiment, right: different force contributions in SIMA).
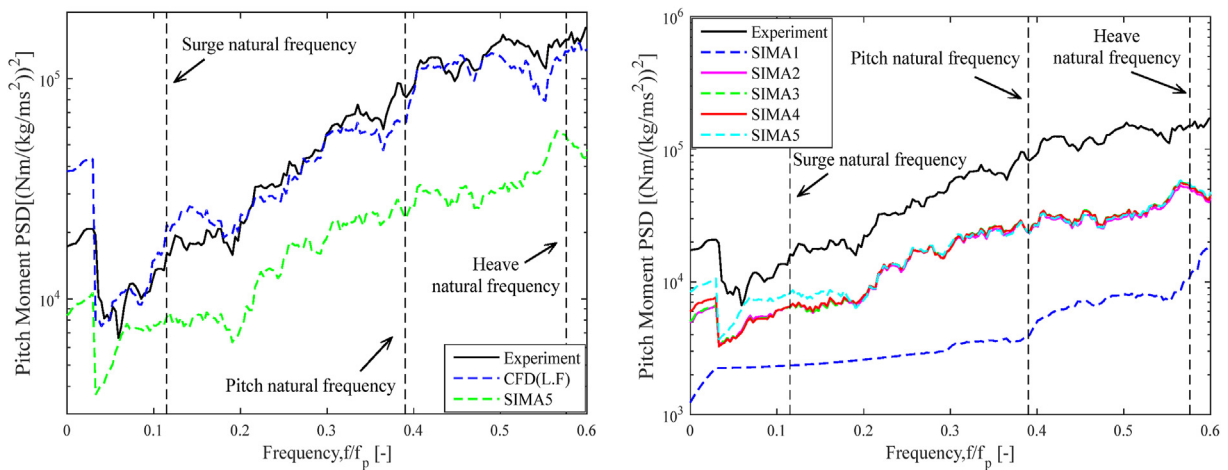
In order to better understand the effects of the multimember arrangement of the semisubmersible, surge forces on each column are extracted. Higher order surge forces on the starboard column are larger than those on the upstream column in the CFD simulations under this regular wave (12.1 s), but this conclusion is frequency-dependent (based on potential flow simulations at additional frequencies). Furthermore, the total surge force on the upper column is larger than the force on the heave plate, and this discrepancy increases for shorter waves.

The effects of 5° mean pitch angle on the nonlinear wave loads are also investigated in regular waves, using the same global coordinate system as in the upright condition. In the trimmed condition, the surge force and pitch moment increase while the heave force decreases. Furthermore, this 5° mean pitch angle reduces the higher order surge and heave forces while increasing the higher order pitch moment. In SIMA, the axial drag forces on the heave plates increase the third harmonic heave force and pitch moment, but decrease the third harmonic surge force, which is due to the phase difference between vertical and horizontal water particle velocity. Considering the effect of changed volume, the surge and heave forces decrease, and the pitch moment slightly increases under trimmed position.

CRediT authorship contribution statement

Haoran Li: Conceptualization, Methodology, Software, Validation, Investigation, Formal analysis, Data curation, Writing – original draft. **Erin E. Bachynski:** Conceptualization, Methodology, Resources, Writing – review & editing, Supervision.

Declaration of competing interest

The authors declare that they have no known competing financial interests or personal relationships that could have appeared to influence the work reported in this paper.

Acknowledgements

References

[1] J.A. Mercier, S.J. Leverette, A.L. Bliault, Evaluation of Hutton TLP response to environmental loads, in: Offshore Technology Conference, 1982. Offshore Technology Conference.

[2] A.J. Coulling, et al., Importance of Second-Order Difference-Frequency Wave-Diffraction Forces in the Validation of a FAST Semi-submersible Floating Wind Turbine Model. No. NREL/CP-5000-57697, in: ASME 2013 32nd International Conference on Ocean, Offshore and Arctic Engineering, American Society of Mechanical Engineers Digital Collection, 2013.

[3] A. Robertson, et al., Offshore Code Comparison Collaboration Continuation within IEA Wind Task 30: Phase II Results Regarding a Floating Semisubmersible Wind System. No. NREL/CP-5000-61154, in: ASME 2014 33rd International Conference on Ocean, Offshore and Arctic Engineering, American Society of Mechanical Engineers Digital Collection, 2014.

[4] A.N. Robertson, et al., OC5 Project Phase I: Validation of Hydrodynamic Loading on a Fixed Cylinder, National Renewable Energy Lab.(NREL), Golden, CO (United States), 2015. No. NREL/CP-5000-63567.

[5] A.N. Robertson, et al., OC5 project phase II: validation of global loads of the DeepCwind floating semisubmersible wind turbine, Energy Procedia 137 (2017) 38–57.

[6] E.E. Bachynski, T. Moan, Ringing loads on tension leg platform wind turbines, Ocean Eng. 84 (2014) 237–248.

[7] M. Karimirad, T. Moan, Wave-and wind-induced dynamic response of a spar-type offshore wind turbine, J. Waterw. Port, Coast. Ocean Eng. 138 (1) (2012) 9–20.

[8] F. Beyer, M. Arnold, P.W. Cheng, Analysis of Floating Offshore Wind Turbine Hydrodynamics Using Coupled CFD and Multibody Methods, 2013.

[9] M.A. Benitz, et al., Validation of Hydrodynamic Load Models Using CFD for the OC4-DeepCwind Semisubmersible. No. NREL/CP-5000-63751, in: ASME 2015 34th International Conference on Ocean, Offshore and Arctic Engineering, American Society of Mechanical Engineers Digital Collection, 2015.

[10] M.A. Benitz, et al., Comparison of Hydrodynamic Load Predictions between Reduced Order Engineering Models and Computational Fluid Dynamics for the Oc4-Deepcwind Semi-submersible. No. NREL/CP-5000-61157, in: ASME 2014 33rd International Conference on Ocean, Offshore and Arctic Engineering, American Society of Mechanical Engineers Digital Collection, 2014.

[11] I. Rivera-Arreba, et al., Modeling of a semisubmersible floating offshore wind platform in severe waves, J. Offshore Mech. Arctic Eng. 141 (6) (2019).

[12] A. Nematbakhsh, D.J. Olinger, G. Tryggvason, A nonlinear computational model of floating wind turbines, J. Fluid Eng. 135 (12) (2013).

[13] A. Nematbakhsh, et al., Comparison of wave load effects on a TLP wind turbine by using computational fluid dynamics and potential flow theory approaches, Appl. Ocean Res. 53 (2015) 142–154.

[14] A. Nematbakhsh, D. Olinger, G. Tryggvason, Development and Validation of a Computational Model for Floating Wind Turbine Platforms. In *50th AIAA Aerospace Sciences Meeting Including the New Horizons Forum and Aerospace Exposition*, 2012.

[15] C. Hu, et al., Hydrodynamic analysis of a semi-submersible type floating wind turbine, in: The Eleventh ISOPE Pacific/Asia Offshore Mechanics Symposium., International Society of Offshore and Polar Engineers, 2014.

[16] C. Liu, C. Hu, CFD simulation of a floating wind turbine platform in rough sea conditions, in: The Twenty-Fourth International Ocean and Polar Engineering Conference, International Society of Offshore and Polar Engineers, 2014.

[17] T. Yabe, F. Xiao, T. Utsumi, The constrained interpolation profile method for multiphase analysis, J. Comput. Phys. 169 (2) (2001) 556–593.

[18] F. Xiao, S. Ii, C. Chen, Revisit to the THINC scheme: a simple algebraic VOF algorithm, J. Comput. Phys. 230 (19) (2011) 7086–7092.

[19] W. Musial, S. Butterfield, A. Boone, Feasibility of floating platform systems for wind turbines, in: t42nd AIAA Aerospace Sciences Meeting and Exhibi, 2004.

[20] A. Robertson, et al., OC6 Phase I: investigating the underprediction of low-frequency hydrodynamic loads and responses of a floating wind turbine, in: TORQUE, 2020.

[21] A.J. Goupee, et al., Model tests for three floating wind turbine concepts, in: Offshore Technology Conference, 2012. Offshore Technology Conference.

[22] H.G. Weller, et al., A tensorial approach to computational continuum mechanics using object-oriented techniques, Comput. Phys. 12 (6) (1998) 620–631.

[23] N.G. Jacobsen, D.R. Fuhrman, J. Fredsøe, A wave generation toolbox for the open-source CFD library: OpenFoam®, Int. J. Numer. Methods Fluid. 70 (9) (2012) 1073–1088.

[24] A.P. Engsig-Karup, H.B. Bingham, O. Lindberg, An efficient flexible-order model for 3D nonlinear water waves, J. Comput. Phys. 228 (6) (2009) 2100–2118.

[25] B.T. Paulsen, H. Bredmose, H.B. Bingham, An efficient domain decomposition strategy for wave loads on surface piercing circular cylinders, Coast Eng. 86 (2014) 57–76.

[26] C.W. Hirt, B.D. Nichols, Volume of fluid (VOF) method for the dynamics of free boundaries, J. Comput. Phys. 39 (1) (1981) 201–225.

[27] E. Berberović, et al., Drop impact onto a liquid film of finite thickness: dynamics of the cavity evolution, Phys. Rev. 79 (3) (2009), 036306.

[28] M.M. Rahman, M.M. Karim, M.A. Alim, Numerical investigation of unsteady flow past a circular cylinder using 2-D finite volume method, J. Nav. Architect. Mar. Eng. 4 (1) (2007) 27–42.

[29] S.A. Brown, et al., An evaluation of rans turbulence closure models for spilling breakers, Coast. Eng. Proc. (34) (2014), 5-5.

[30] F. Menter, et al., The SST turbulence model with improved wall treatment for heat transfer predictions in gas turbines, in: Proceedings of the International Gas Turbine Congress, 2003.

[31] B. Devolder, P. Rauwoens, P. Troch, Application of a buoyancy-modified k-ω SST turbulence model to simulate wave run-up around a monopile subjected to regular waves using OpenFOAM®, Coast Eng. 125 (2017) 81–94.

[32] W. Fan, H. Anglart, varRhoTurbVOF, A new set of volume of fluid solvers for turbulent isothermal multiphase flows in OpenFOAM, Comput. Phys. Commun. 247 (2020) 106876.

[33] T.T. Tran, D.-H. Kim, The coupled dynamic response computation for a semi-submersible platform of floating offshore wind turbine, J. Wind Eng. Ind. Aerod. 147 (2015) 104–119.

[34] S. Dudley Brian, A single formula for the "law of the wall, J. Appl. Mech. 28 (3) (1961) 455–458.

[35] N. Bruinsma, B. Paulsen, N. Jacobsen, Validation and application of a fully nonlinear numerical wave tank for simulating floating offshore wind turbines, Ocean Eng. 147 (2018) 647–658.

[36] L. Eça, M. Hoekstra, A procedure for the estimation of the numerical uncertainty of CFD calculations based on grid refinement studies, J. Comput. Phys. 262 (2014) 104–130.

[37] L. Eça, M. Hoekstra, On the influence of the iterative error in the numerical uncertainty of ship viscous flow calculations, in: 26th Symposium on Naval Hydrodynamics, Italy, Rome, 2006.

[38] Marintek, SIMO—Theory Manual Version 4.0, Marintek Trondheim, Norway, 2012.

[39] H. Ormberg, E. Passano, RIFLEX Theory Manual, Marintek, Trondheim, 2012.

[40] C.-H. Lee, WAMIT Theory Manual, Massachusetts Institute of Technology, Department of Ocean Engineering, 1995.

[41] A. Robertson, et al., Definition of the Semisubmersible Floating System for Phase II of OC4. No. NREL/TP-5000-60601, National Renewable Energy Lab.(NREL), Golden, CO (United States), 2014.

[42] A. Robertson, et al., Total experimental uncertainty in hydrodynamic testing of a semisubmersible wind turbine, considering numerical propagation of systematic uncertainty, Ocean Eng. 195 (2020) 106605.

[43] K.H. Halse, On Vortex Shedding and Prediction of Vortex-Induced Vibrations of Circular Cylinders, Norwegian University of Science and Technology, 1997.

[44] E.E. Bachynski, et al., Computational fluid dynamics reproduction of nonlinear loads on a vertical column during extreme irregular wave events, J. Offshore Mech. Arctic Eng. 140 (6) (2018).